Title

Three-dimensional simultaneous brain mapping of T1, T2, and magnetic susceptibility with MR Multitasking

Journal

Magnetic Resonance in Medicine, 87(3)

ISSN

0740-3194

Authors

Cao, Tianle
Ma, Sen
Wang, Nan
et al.

Publication Date

2022-03-01

DOI

10.1002/mrm.29059

Peer reviewed

HHS Public Access

Author manuscript

Magn Reson Med. Author manuscript; available in PMC 2023 March 01.

Published in final edited form as:

Magn Reson Med. 2022 March ; 87(3): 1375–1389. doi:10.1002/mrm.29059.

Three-dimensional Simultaneous Brain Mapping of T1, T2, T2*, and Magnetic Susceptibility with MR Multitasking

Tianle Cao[1,2], **Sen Ma**[1], **Nan Wang**[1], **Sara Gharabaghi**[3], **Yibin Xie**[1], **Zhaoyang Fan**[1,4], **Elliot Hogg**[5], **Chaowei Wu**[1,2], **Fei Han**[6], **Michele Tagliati**[5], **E. Mark Haacke**[3,7,8], **Anthony G. Christodoulou**[1,2], **Debiao Li**[1,2,*]

[1]Biomedical Imaging Research Institute, Cedars-Sinai Medical Center, Los Angeles, California, USA

[2]Department of Bioengineering, University of California, Los Angeles, California, USA

[3]Magnetic Resonance Innovations, Inc., Bingham Farms, MI, USA

[4]Department of Radiology, Keck School of Medicine, University of Southern California, Los Angeles, California, USA

[5]Department of Neurology, Cedars-Sinai Medical Center, Los Angeles, California, USA

[6]Siemens Medical Solutions USA, Inc., Los Angeles, California, USA

[7]Department of Radiology, Wayne State University School of Medicine, Detroit, MI, USA

[8]The MRI Institute for Biomedical Research, Bingham Farms, MI, USA

Abstract

Purpose: To develop a new technique that enables simultaneous quantification of whole brain T1, T2, T2*, as well as susceptibility and synthesis of six contrast-weighted images in a single 9.1min scan.

Methods: The technique employs hybrid T2-prepared inversion recovery (T2-IR) pulse modules and multi-echo gradient echo (GRE) readouts to collect k-space data with various T1, T2 and T2* weightings. The underlying image is represented as a six-dimensional low-rank tensor consisting of three spatial dimensions and three temporal dimensions corresponding to T1 recovery, T2 decay, and multi-echo behaviors respectively. Multiparametric maps were fitted from reconstructed image series. The proposed method was validated on phantoms and healthy volunteers, by comparing quantitative measurements against corresponding reference methods. The feasibility of generating six contrast-weighted images was also examined.

Results: High quality, co-registered T1/T2/T2*/susceptibility maps were generated that closely resembled the reference maps. Phantom measurements showed substantial consistency (R^2>0.98) with the reference measurements. Despite the significant differences of T1 (P<0.001), T2 (P=0.002), and T2* (P=0.008) between our method and the references for in-vivo studies, excellent agreement was achieved with all intraclass correlation coefficients greater than 0.75.

*Correspondence to: Debiao Li, PhD, Biomedical Imaging Research Institute, Cedars-Sinai Medical Center, 8700 Beverly Blvd, PACT 400, Los Angeles, CA 90048, USA, debiao.li@cshs.org.

No significant difference was found for susceptibility (P=0.900). The framework is also capable of synthesizing six contrast-weighted images.

Conclusion: MR Multitasking based 3D brain mapping of T1, T2, T2*, and susceptibility agrees well with the reference and is a promising technique for multi-contrast and quantitative imaging.

Keywords

MR studies; brain; MR Multitasking; quantitative MRI; multiparametric mapping

1. Introduction

MRI offers flexible contrast between different brain tissues based on their distinct physical properties including proton density, longitudinal relaxation time (T1), transverse relaxation times (T2, T2*), and magnetic susceptibility (χ). Compared to qualitative or contrast-weighted images, quantitative imaging provides objective information for tissue characterization and clinical diagnosis. Direct measurement of the above parameters facilitates pathology detection such as tumor (1), ischemia (2), multiple sclerosis (3,4), and Parkinson's disease (5,6). Compared to single parameter mapping, multiparametric approaches offer the potential for more comprehensive tissue characterization and more accurate diagnosis. It has been shown that the combination of R2* and susceptibility is useful to characterize heterogeneity in MS lesions (7). Additionally, combined use of R2* and fractional anisotropy has enhanced the sensitivity and specificity in differentiating Parkinson's disease (PD) patients from healthy controls (8).

In practice, multiparametric mapping typically requires separate scans. Different methods, including inversion recovery spin echo (IRSE), variable flip angle (VFA) (9), multi-echo spin-echo (10), and multi-echo GRE (11–14), have been proposed to measure T1, T2, T2*, and susceptibility independently. Separate acquisitions may result in prolonged scan time, complicated imaging workflows, and misaligned parameter maps due to inter-scan misregistration. Recent technical developments have enabled simultaneous, multiparametric mapping. STrategically Acquired Gradient Echo (STAGE) (15–17) achieves T1, T2*, and quantitative susceptibility mapping (QSM) using two multi-echo GRE sequences with different flip angles, but lacks T2 quantification and requires B1 inhomogeneity correction. Multi-Echo (ME) Magnetization-Prepared 2 RApid Gradient Echoes (MP2RAGE) (18–20) uses two different inversion times each with a unique flip angle and with multi-echo GRE readouts for T1, T2*, and susceptibility quantification. However, the evolution of the magnetization during the long acquisition window results in distortion of the point-spread function and causes blurring (21,22). In addition, it does not perform flow compensation and would therefore be subject to phase errors from flow effects (11). Recent MR fingerprinting work combines the existing balanced SSFP methods with varied RF excitation phases for simultaneous quantification of T1, T2, and T2*, yet is limited by 2D acquisition, banding artifacts, and long acquisition time (35s per slice) (23).

In this work, we develop a new technique for 3D whole-brain simultaneous T1, T2, T2*, and susceptibility quantification in a single 9.1 min scan, based on the MR Multitasking framework. Hybrid T2-IR preparations generate different T1 and T2 weightings, while

multi-echo GRE readouts with full flow compensation for all echoes generate different T2* weightings. The underlying image is modeled as a six-dimensional low rank tensor (LRT) with three spatial dimensions and three temporal dimensions modelling T1, T2, and T2* relaxations. In addition, we also show six contrast-weighted images that can be generated from the T1/T2/T2*/susceptibility maps. The agreement between the proposed method and conventionally accepted quantitative reference mapping techniques for each tissue property is evaluated in phantom and volunteer studies.

2. Methods

2.1 Pulse sequence framework

2.1.1 Pulse sequence—Figure 1 shows the proposed sequence diagram. T1 and T2 weightings are generated by cycling through T2-IR preparations with four different preparation durations (τ, with $\tau = 0$ corresponding to a standard IR pulse). Multi-echo GRE readouts with different echo times (T_E) produce different T2* weightings and images with different susceptibility contributions. FLASH excitations fill the entire recovery period to acquire readouts at multiple inversion times (T_I).

Flow induced phase variation can be a potential source of error when quantifying susceptibility (11). Available multi-echo sequences typically only perform flow compensation on the first echo (24). Failure to compensate the flow may lead to arbitrary phase inside the vessels and non-local artifacts in susceptibility maps (25,26). In this work, we adopt a previously proposed flow compensation scheme (26) for 3D monopolar multi-echo acquisition, where extra bipolar pairs are implemented along both phase encoding and partition encoding directions (Figure 1B). In the readout direction, insertion of an appropriate gradient before the first echo can naturally achieve the flow compensation at the center of each echo.

Two interleaved subsets of data are collected during a continuous acquisition (Figure 1C): training data $\mathbf{d}_{\text{tr}}$ which frequently repeat one **k**-space trajectory with a high temporal sampling rate, and imaging data $\mathbf{d}_{\text{img}}$ which sparsely sample ($\mathbf{k}$,t)-space with greater **k**-space extent for high spatial resolution. The imaging data densely sample ($\mathbf{k}$,t)-space for the chosen **k**-space trajectory, and will therefore allow the calculation of a highly temporally-resolved subspace of plausible contrast-weighting evolutions during image reconstruction; in this work, $\mathbf{d}_{\text{tr}}$ was collected at the central **k**-space line $k_y = k_z = 0$) every 4 readouts (~ 80ms). The imaging data then allow high-resolution calculation of voxelwise contrast-weighting evolution within the temporal subspace; here, $\mathbf{d}_{\text{img}}$ was collected using a 3D randomly-ordered trajectory with Gaussian density distribution along both partition and phase encoding directions in order to provide incoherent ($\mathbf{k}$, t)-space sampling.

2.1.2 Image model—The Multitasking framework models the underlying image as a 6D image $x(\mathbf{r}, \tau, T_I, T_E)$ with 3 spatial dimensions indexed by $\mathbf{r}$ $[x,y,z]$, and 3 temporal dimensions τ, T_{I}, and T_{E}. Here τ is the T2-IR prep duration, T_I is the inversion time, and T_E is the echo time. Acquisition of image x at the Nyquist rate would suffer from the curse of dimensionality and result in an impractical scan time. However, x can still be recovered from highly undersampled data by exploiting the spatial-temporal correlation throughout the

image. Specifically, this correlation allows x to be decomposed into the following partially separable form (27):

$$x(\mathbf{r},\tau,T_I,T_E)=\sum_{l=1}^{L}u_l(\mathbf{r})\phi_l(\tau,T_I,T_E) \tag{1}$$

where $\{u_l(\mathbf{r})\}_{l=1}^{L}$ are the spatial basis functions and $\{(\phi_l(\tau,T_I,T_E)\}_{l=1}^{L}$ are temporal functions spanning a multi-dimensional temporal subspace. The temporal functions $\boldsymbol{\phi}$ themselves can also be decomposed in terms of individual bases along each temporal dimension, e.g.:

$$\phi_l(\tau,T_I,T_E)=\sum_{m=1}^{M}\sum_{n=1}^{N}\sum_{p=1}^{P}g_{lmnp}v_m(\tau)w_n(T_I)q_p(T_E), \tag{2}$$

where $\{v_m(\tau)\}_{m=1}^{M},\{w_n(T_\mathrm{I})\}_{n=1}^{N},\{q_p(T_\mathrm{E})\}_{p=1}^{P}$ are temporal basis functions for T2, T1, and T2* relaxation dimensions and where g_{lmnp} are elements of a core tensor $\mathcal{G}$ (28). The combination of Equations (1) and (2) implies that a discretized image tensor $\mathcal{X}$ with elements $x_{ijks}=\mathbf{r}_i,\boldsymbol{\tau}_j,T_{\mathrm{I},k},T_{E,s})$ can be decomposed in Tucker form (29,30) as follows:

$$\mathcal{X}=\mathcal{G}\times_1\mathbf{U}\times_2\mathbf{V}\times_3\mathbf{W}\times_4\mathbf{Q}, \tag{3}$$

where the $\times_i$ operator denotes the ith mode product (30), the columns of **U** contain the spatial basis functions such that $\mathbf{U}_{i,l}=u_l(\mathbf{r}_i)$, and the columns of **V**, **W**, and **Q** contain the temporal basis functions for each corresponding dimension such that $\mathbf{V}_{j,m}=v_m(\boldsymbol{\tau}_j)$, $\mathbf{W}_{k,n}=w_n(T_{\mathrm{I},k})$, $\mathbf{Q}_{s,p}=q_p(T_{\mathrm{E},s})$. By separating the temporal factors **V**, **W**, and **Q** from the spatial factor **U**, the model in Equation (3) partially decouples conflicting temporal and spatial resolution sampling requirements: the high-speed training data in $\mathbf{d}_{\mathrm{tr}}$ can be used to determine the temporal factors, and the $\mathbf{d}_{\mathrm{img}}$ (which extensively covers k-space) can be used to determine **U** with high spatial resolution. The end result is an $\mathcal{X}$ that is both highly spatially- and temporally-resolved.

2.1.3 Image reconstruction—Equation (3) implies that the 4-way tensor $\mathcal{X}$ can be recovered from undersampled $(\mathbf{k},\boldsymbol{\tau},T_\mathrm{I},T_\mathrm{E})$-space data via low-rank tensor completion. For example, this could in principle be done by solving the following optimization problem:

$$\widehat{\mathcal{X}}=\arg\min_{\mathcal{X}}\left\|\mathbf{d}_{\mathrm{img}}-\Omega(\mathcal{X}\times_1\mathbf{FS})\right\|_2^2+\lambda\sum_{i=1}^{4}\left\|\mathbf{X}_{(i)}\right\|_*+R\left(\mathcal{X}\right), \tag{4}$$

where $\mathbf{d}_{\mathrm{img}}$ is the imaging data, $\Omega(\cdot)$ is the sampling operator, **F** represents the Fourier transform, **S** applies sensitivity maps, λ is the rank regularization parameter, $\mathbf{X}_{(i)}$ denotes the i-mode matrix unfolding of $\mathcal{X}$ (i ranges from 1 to 4 as $\mathcal{X}$ is a 4-way tensor), $\|\cdot\|_*$ denotes the matrix nuclear norm, and $R(\cdot)$ is an optional regularizer which can be employed to enforce complementary image properties such as transform sparsity.

Although Equation (4) can be a potential solution, implementing it can be impractical owing to the large memory consumption in storing and operating upon the entire $\mathcal{X}$ without taking advantage of the decomposition in Equation (3) (31). Instead of solving Equation (4), we employ a computationally-efficient practical alternative to reconstruct $\mathcal{X}$ in factored form, e.g., solving directly for an individual parameter such as $\mathbf{U}$:

$$\widehat{\mathbf{U}} = \arg\min_{\mathbf{U}} \left\| \mathbf{d}_{\text{img}} - \Omega\left(\widehat{\boldsymbol{\Phi}} \times_1 \mathbf{FSU}\right) \right\|_2^2 + \lambda R_s(\mathbf{U}) \tag{5}$$

for known temporal factor tensor $\widehat{\boldsymbol{\Phi}} = \mathcal{G} \times_2 \mathbf{V} \times_3 \mathbf{W} \times_4 \mathbf{Q}$, where $R_s(\cdot)$ is a spatial regularizer, chosen as a total variation (TV) penalty for this study. Note that the required "prior" knowledge of $\widehat{\boldsymbol{\Phi}}$ can be obtained in two steps: (1) predetermine the T1 recovery basis functions in $\mathbf{W}$ from a dictionary of IR signal curves; and (2) estimate the T2 relaxation basis functions in $\mathbf{V}$, T2* relaxation basis function in $\mathbf{Q}$, and core tensor $\mathcal{G}$ from the training data $\mathbf{d}_{\text{tr}}$.

In the first step, we generate a dictionary of physically feasible IR-GRE signal curves for a range of feasible T1 and B1 inhomogeneity values based on the Bloch equations (31). The dictionary consists of 101 T1 values logarithmically spaced from 100 ms to 3000 ms, 24 flip angles equally spaced between 0.5° to 12°, and 21 inversion efficiency factors equally spaced between −1 (perfect inversion) and −0.5. The T1 recovery basis functions in $\mathbf{W}$ are estimated from the singular value decomposition (SVD) of this training dictionary.

In the second step, the training tensor $\mathcal{D}_{\text{tr}}$, as expressed in $(\mathbf{k}, \boldsymbol{\tau}, T_{\text{I}}, T_{\text{E}})$-space, can still be incomplete. However, it has much smaller size than the imaging data and can be recovered in a similar fashion as in Equation (4):

$$\widehat{\mathcal{D}}_{\text{tr}} = \underset{\mathcal{D}_{\text{tr}}}{\text{argmin}} \|\mathbf{d}_{\text{tr}} - \Omega_{\text{tr}}(\mathcal{D}_{\text{tr}})\|_2^2 + \lambda \sum_{i=1}^{4} \|\mathbf{D}_{\text{tr},(i)}\|_*, \tag{6}$$

where $\mathbf{d}_{\text{tr}}$ is the training data, $\Omega_{\text{tr}}(\cdot)$ is the sampling operator for the training dataset, and $\mathbf{d}_{\text{tr,(i)}}$ denotes the i-mode matrix unfolding of $\mathcal{D}_{\text{tr}}$ (i ranges from 1 to 4 as $\mathcal{D}_{\text{tr}}$ is a 4-way tensor). Note Equation (6) is practical to solve, as $\mathcal{D}_{\text{tr}}$ is of much smaller size than $\mathcal{X}$ and does not need to be encoded by the Fourier transform and coil sensitivities as in Equation (4). Once the completed $\widehat{\mathcal{D}}_{\text{tr}}$ has been recovered, the core tensor $\mathcal{G}$, T2 basis functions $\mathbf{V}$, and T2* basis functions $\mathbf{Q}$ can be extracted by truncating the high-order SVD (HOSVD)(32) of $\widehat{\mathcal{D}}_{\text{tr}}$. This allows the spatial basis $\widehat{\mathbf{U}}$ to be solved as described in Equation (5). The final reconstructed tensor is then given by the product $\widehat{\mathcal{X}} = \widehat{\boldsymbol{\Phi}} \times_1 \widehat{\mathbf{U}}$.

In this work we follow the approach in Equations (5) and (6). The low-rank tensor modelling of the image series and reconstruction workflow can be found in Figure 2.

2.1.4 Parameter quantification—

Multiparametric fitting was based on the following equation at a given T2-IR preparation time ($\boldsymbol{\tau}$), *nth* readout index since preparation (i.e., n=1,

2, …, N_{seg}, where N_{seg} denotes the number of segments within one recovery period, such that $T_I = nT_R$) and echo time (T_E):

$$S = A\frac{1-e^{-T_R/T_1}}{1-e^{-T_R/T_1}\cos\alpha}\left[1+\left(Be^{-\tau/T_2}-1\right)\left(e^{-T_R/T_1}\cos\alpha\right)^n\right]e^{-T_E/T_2^*}e^{j2\pi\Delta B_0 T_E}\sin\alpha \quad (7)$$

where A absorbs proton density (equilibrium magnetization M_0) and receiver coil sensitivity, B represents the effective inversion efficiency independent of T_2 (with $B = -1$ being perfect), ΔB_0 describes the effect of static field inhomogeneity in Hz, T_R is the repetition time, and α denotes the flip angle. Nonlinear least squares-fitting was performed on the three-way tensor reconstructed at each voxel using Equation (7) for A, T_1, T_2, T_2^*, B, and ΔB_0.

Magnetic susceptibility was estimated using the multi-echo images at different echo time T_E of the last inversion time (n=N_{seg}), closest to the GRE steady-state contrast. Phase images at different echo times were unwrapped using the quality guided 3D phase unwrapping algorithm (33). After that, brain regions were masked with a brain extraction tool (BET) (34) and background field was removed using Sophisticated Harmonic Artifact Reduction for Phase data (SHARP) (35). Individual QSM images were generated at each echo using iterative susceptibility weighted Imaging and mapping (iSWIM) method (36,37) with 4 iterations and threshold of 0.15. Finally, they were combined using a weighted averaging method (38):

$$\chi = \frac{\sum_{i=1}^{3} M_i^2 \chi_i}{\sum_{i=1}^{3} M_i^2} \quad (8)$$

where χ_i is the susceptibility estimated at echo time $T_{E,i}$, and $M_i = T_{E,i}e^{-T_{E,i}/T2^*}$.

2.2 Data acquisition

2.2.1 MR Multitasking imaging protocol—MRI experiments were performed on a 3T scanner (Biograph mMR, Siemens Healthineers, Erlangen, Germany) with a 20-channel head coil. Acquisition cycled through hybrid T2IR modules with preparation times τ = 0, 30, 55, 80 ms. Within each readout module, three echo times at T_E = 5.0, 10.0, 16.25 ms were collected. The scan time for Multitasking was 9.1 min. Scan parameters for Multitasking were: field of view (FOV) = 276 × 207 mm^2, in-plane resolution = 0.7 × 1.4 mm^2, slice thickness = 2 mm. More detailed imaging protocol was summarized in Table 1.

2.2.2 Phantom study—A standard T1/T2/T2* phantom (Calimetrix, Madison, WI USA) was scanned for validation of the quantitative estimates of the tissue properties. Inversion-recovery spin echo (IR-SE), T2-weighted spin echo (T2-SE) and 3D multi echo gradient echo (ME-GRE) were used as the reference for T1, T2 and T2* respectively.

Another susceptibility phantom was constructed by embedding 5 different falcon tubes, each filled with different concentrations (0, 1, 3, 5, or 7 mmol/L) of gadolinium (OptiMARK, Liebel-Flarsheim Company, Raleigh, NC) solution, into a 1% agarose gel solution in a 1000

mL plastic container. The phantom was scanned with Multitasking and reference (ME-GRE) sequences.

Imaging parameters for all reference sequences are summarized in Supporting Information Table S1.

2.2.3 In-vivo study—The in-vivo study was approved by the institutional review board at Cedars-Sinai Medical Center. Written informed consent from all subjects were obtained before the study. $N = 10$ healthy volunteers (age: 41.9 ± 14.6) were recruited. The reference protocols included inversion recovery turbo spin echo (IR-TSE) for T1 mapping, multi-echo spin echo (ME-SE) for T2 mapping, and 3D fully flow-compensated multi-echo gradient echo (ME-GRE) for T2*/QSM mapping, with a total scan time of 20 min. These references were chosen from previous work on T1/T2/T2*/susceptibility mapping (12,19,39–43). Note that the T1/T2 mapping references were different from those used in the phantom study and had smaller spatial coverage to make scan time feasible. Detailed parameters are listed in Supporting information Table S2. The slice positions of all scans matched with each other.

MR Multitasking reconstruction was performed using Equation (5) and (6), where TV was used as a regularizer. The ranks for spatial and T1 dimensions were chosen from the −40 dB threshold on the normalized singular value curves of the training data and simulated dictionary, respectively. The rank for T2 dimension was not truncated as the nuclear norm term in Equation (6) for training tensor completion already performed a soft constraint on the tensor ranks of those dimensions. Finally, the multi-echo dimension was considered as full rank to account for both T2* decay and B0 field inhomogeneity.

For comparison purposes, a compressed sensing reconstruction with TV regularizer, a non-regularized low-rank tensor reconstruction (i.e., Equation (5) with $\lambda = 0$), and our proposed TV-regularized low-rank reconstruction were performed for several representative T1/T2/T2* contrast combinations on a healthy subject. For the compressed sensing reconstruction, the k-space data along the T1 dimension were grouped into 8 different inversion times (more typical of conventional T1 mapping techniques), leading to an acceleration factor of 12.

The MATLAB p-code for the reconstruction is available upon reasonable request.

2.3 Image processing and assessment

2.3.1 Contrast-weighted image generation—Contrast-weighted images were synthesized by substituting the quantitative parameters into the signal equations for common MRI pulse sequences. The sequences used for synthesizing T1, T2-weighted, double inversion recovery (DIR), and T2 fluid-attenuated inversion recovery (FLAIR) images are listed in Supporting information Table S4.

Note that some contrast-weighted images may not need to be re-synthesized using signal equations if they are already available in the reconstructed image series prior to parameter fitting. For example, a T1-weighted image can be directly obtained by choosing the reconstructed image at the desired inversion time.

For susceptibility-weighted images (SWI), phase masks are created from the high-pass filtered raw phase images and are multiplied by the magnitude images (44). True susceptibility-weighted images (tSWI) have also been generated by using susceptibility maps for the masking process (45). tSWI can enhance the contrast and overcome the limitation of SWI, where the phase images used for masking are dependent not only on susceptibility, but also on shape and orientation of the structure of interest (45). Both SWI and tSWI are displayed using minimum intensity projections (MinIPs) with an effective slab thickness of 16mm (8 slices). Parameters used for masking are also listed in Supporting information Table S3.

2.3.2 Qualitative analysis—All reconstructions were performed on a Linux workstation with a 3.08-GHz dual 16-core Intel Xeon processor equipped with 256 GB RAM and running MATLAB 2016b (MathWorks, Natick, Massachusetts). After finishing the reconstruction, three slices located in the upper, middle and lower brain regions were selected for each healthy subject for multiparametric fitting using Equation (7). The generated T1/T2/T2* maps were compared with the corresponding reference maps. Additionally, two slices around subcortical regions were chosen for qualitative evaluation of QSM, SWI, and tSWI.

2.3.3 Quantitative analysis—For the phantom study, T1/T2/T2*/susceptibility measurements were calculated for each vial. Linear regression was preformed and intraclass correlation coefficients (ICCs) were calculated from a two-way mixed model and 95% confidence using IBM SPSS Statistics (Armonk, New York) to evaluate the agreement between Multitasking and the reference.

For the volunteer study, regions of interest (ROIs) were drawn for cortical GM and WM in both left and right hemisphere for all healthy volunteers. The segmentation was performed by thresholding raw reference/Multitasking images at approximately similar slice locations (46). Mean T1/T2/T2* values of cortical GM and WM were calculated and compared between Multitasking and the references. In addition, three different subcortical areas (substantia nigra, red nucleus and globus pallidus) were manually labelled for comparison of susceptibility maps. Bland-Altman analysis was performed and coefficient of variation (CV) and ICCs from a two-way mixed model and 95% confidence were calculated to test the agreement between different methods. Two-way repeated measures analysis of variance (ANOVA) was performed using IBM SPSS Statistics (Armonk, New York) to determine the differences between Multitasking and reference.

3. Results

3.1 Phantom study

Multitasking T1/T2/T2* maps showed good quality and qualitative agreement with the reference maps (Figure 3). Substantial correlation (R^2 = 0.997, 0.997, and 0.999 for T1/T2/T2*, respectively) and excellent agreement (ICC = 0.991, 0.990, and 0.997 for T1/T2/T2*, respectively) were found between Multitasking measurements and the reference measurements.

The susceptibility maps from Multitasking and reference were shown in Figure 4A, with the gadolinium (Gd) concentration (in mmol/L) of each vial labelled in the magnitude image. Both maps had good image quality and resembled each other. The correlation plot in Figure 4B showed good consistency between Multitasking and reference (R^2=0.988, ICC = 0.994). The susceptibility measurements from Multitasking also correlated well with the Gd concentration (Figure 4C), yielding a slope of 0.338 ppm per mmol/L. This is consistent with previous literature on Gd phantom (0.326 – 0.350 ppm per mmol/L) (47–49).

3.2 In-vivo study

Representative images with different contrast combinations reconstructed by compressed sensing only, low-rank only, and low-rank with compressed sensing (our proposed method) were shown in Supporting Information Figure S1. The high acceleration factor made reconstruction challenging for compressed sensing and the results showed poor image quality and aliasing artifacts. Low-rank tensor reconstruction generated aliasing-free images but were noisy, especially for images at short T_1. The proposed reconstruction taking advantage of both the low-rank property and spatial regularization had the best image quality with minimal noise and aliasing.

As shown in Figure 5, Multitasking generated co-registered multiparametric maps qualitatively matched with the reference ones. Bland-Altman plots for T1/T2/T2* were shown in Figure 6A–C. Compared with reference methods, Multitasking values are 6% higher in T1, 4% lower in T2 and T2*. Supporting information Table S5 provided the results of two-way ANOVA, which showed significant differences among different methods for T1, T2, and T2* ($P \leq 0.008$). The distributions of T1/T2/T2* measurements from the two methods were summarized in Table 2. Despite the differences between the two methods, all the values were still within the ranges from literature (GM T1: 1209–1700 ms; WM T1: 750–1110 ms; GM T2: 71–132 ms; WM T2: 56–84 ms; GM T2*: 40–65 ms; WM T2*: 44–52 ms).(50–56) Additionally, CVs (< 5%) and ICCs (> 0.75) indicated the excellent consistency between Multitasking and reference techniques (57).

Two slices of QSM maps were shown in Figure 7. Both Multitasking and reference maps clearly visualized the deep gray matter structure. The same structures as well as vessels could also be found in MinIPs of SWI and tSWI images. Multitasking qualitatively agreed with reference in all maps and images. Bland-Altman plot for susceptibility shown in Figure 6D indicated little bias between Multitasking and reference methods. As shown in Supporting information Table S4, no significant difference was found between the two methods ($P = 0.900$) with two-way ANOVA. The susceptibility values and their distributions were summarized in Table 2. These measurements were consistent with the reference ones (CV < 5%, ICC > 0.95) and literature values (SN: 0.083–0.115 ppm, RN: 0.076–0.120 ppm, GP: 0.093–0.123 ppm) (6,58–61).

Quantitative maps and six contrast-weighted images of a healthy volunteer were generated from Multitasking and were shown in Figure 8. As a byproduct from Equation (7), static field inhomogeneity ΔB_0 and equilibrium magnetization M_0 were also shown. T1-weighted image synthesized based on the Bloch equations were compared with the one directly taken from reconstructed series in Supporting information Figure S2, which showed very

similar contrast. DIR images with GM, WM, and CSF enhanced separately were shown in Supporting information Figure S3. All images and maps showed appropriate image contrasts.

4. Discussion

In this work, we developed a 3D fully flow-compensated Multitasking T1/T2/T2*/QSM mapping technique. Validation was performed with phantom and volunteer studies. Quantitative in vivo measurements showed substantial agreement between Multitasking and the reference methods. Conventional multiparametric mapping techniques in the brain require separate scans, which is time consuming and can suffer from inter-scan misregistration and intra-scan motion. In comparison, our technique performs co-registered whole brain multiparametric mapping within a single 9.1-min scan and is two times as fast as the reference techniques (20 min) used in this study. The high-dimensional contrast encoding approach in Multitasking has further potential for resolving sub-voxel structure through relaxation correlation spectroscopy (62), which would otherwise become an ill-posed problem with 1D relaxation imaging methods (63–65).

To the best of our knowledge, this is the first technique for whole brain, simultaneous mapping of T1, T2, T2*, and susceptibility. STAGE (15–17) achieves whole brain T1/T2*/QSM mapping at the same resolution within 5 minutes, while multi-echo MP2RAGE technique performs T1/T2*/QSM mapping at a higher resolution (0.64 mm^3) within 16 minutes (20). In a more recent work, the scan time of multi-echo MP2RAGE is shortened to 8.5 minutes (19). However, the choice of very short last TE (~9ms) negatively impacts accuracy of T2* estimation (20). Furthermore, none of the techniques performs T2 quantification, and thus provide incomplete information for brain tissue characterization, as T2-weighted and T2-FLAIR images play a critical role in studying white matter disease and tumor imaging (66–68). And the multitasking approach presented herein offers a distinct advantage. Recent fingerprinting work has achieved joint T1, T2, and T2* mapping, yet has limitations including 2D acquisition, long scan time (35s per slice), and no susceptibility information (23).

Multitasking T1, T2, T2* and QSM maps show good consistency with the references. Nevertheless, small but significant biases were found in T1/T2/T2* measurements between Multitasking and the references. Possible reasons include: (1) IR-TSE is known to underestimate T1 compared to IR-SE due to slice interference (69). (2) T2 differences could be caused by the sensitivity of the Multitasking preparation scheme (T2-IR) to B1 inhomogeneity (70) and the possible overestimation of ME-SE from stimulated echo contamination (71). (3) Remaining phase drifting during a long scan could cause phase cancellation effects, leading to T2* underestimation. Further technical improvements may be able to compensate these effects. Despite the differences, CVs and ICCs still indicate substantial quantitative agreement between the two methods and measurements from both methods were in the range of previous literature.

Six different contrast-weighted images were generated from Multitasking quantitative maps. Although all images show correct contrast, it should be noted that our synthetic FLAIR

image still requires further improvement to match the clinical standards. The challenge of synthesizing T2-FLAIR has also been mentioned by others (72–74) and can be related to partial volume, flow, and magnetization transfer effects. Better results may be obtained with the help of deep learning (72,74). Image synthesis has also been explored by previous MR fingerprinting work and by STAGE (15–17,75). Compared to previous work, Multitasking provides an alternative for certain contrast weighted images. In this work we demonstrate that a decent T1-weighted image can be directly obtained from the reconstructed image series without requiring synthesis. This may help to overcome the challenges related to Bloch synthesis (e.g. flow, magnetization transfer) and produce more 'natural' image contrast.

One future direction for this work is to increase spatial resolution to 1.0 mm isotropic resolution while retaining a reasonable scan time. The current resolution may still cause partial volume effects and missing of small lesions and bleeds. Scan time also limits the choice of TE and TR. The longest TE adopted in the current protocol matches with previous work (15,18), but may still need lengthening to improve estimation for WM and GM T2* values (20). Making this change would result in even longer scan time. Further technical improvement may be made by incorporating other prior knowledge including conjugate symmetry (76) and locally low rankness (77) for a shorter scan. For T2* mapping particularly, B0 inhomogeneity correction along the gradient echo correction may help to improve the low-rank property and further cut down scan time. Deep learning-based methods like super-resolution are also potential avenues to improve spatial resolution (78,79). In this study, we did not investigate the robustness of our sequence to motion, which can be important during a long scan or for pediatric/patient population (80,81). However, we note that the Multitasking framework has been demonstrated to support several motion-handling techniques to produce motion-robust maps (82), such as automatically identifying and removing motion-corrupted data (83,84) or by modelling motion as a separate dimension in the tensor form (31,85,86). Finally, clinical validations would be performed in the future to investigate the usefulness of the technique for diagnostic purposes.

5. Conclusion

We have developed a three-dimensional, whole brain simultaneous T1/T2/T2*/susceptibility mapping method in a single 9.1-min scan based on the MR Multitasking framework. The technique can retrospectively generate six different contrast-weighted images in addition to the four quantitative maps.

Supplementary Material

Refer to Web version on PubMed Central for supplementary material.

Acknowledgements

This work was supported by NIH 1R01EB028146. Anthony G. Christodoulou and Debiao Li contributed equally to this work.

7. References

1. Lescher S, Jurcoane A, Veit A, Bahr O, Deichmann R, Hattingen E. Quantitative T1 and T2 mapping in recurrent glioblastomas under bevacizumab: earlier detection of tumor progression compared to conventional MRI. Neuroradiology 2015;57(1):11–20. [PubMed: 25287076]
2. Steen RG, Hunte M, Traipe E, Hurh P, Wu S, Bilaniuk L, Haselgrove J. Brain T1 in young children with sickle cell disease: evidence of early abnormalities in brain development. Magn Reson Imaging 2004;22(3):299–306. [PubMed: 15062925]
3. Vrenken H, Geurts JJG, Knol DL, van Dijk LN, Dattola V, Jasperse B, van Schijndel RA, Polman CH, Castelijns JA, Barkhof F, Pouwels PJW. Whole-brain T1 mapping in multiple sclerosis: Global changes of normal-appearing gray and white matter. Radiology 2006;240(3):811–820. [PubMed: 16868279]
4. Stevenson VL, Parker GJ, Barker GJ, Birnie K, Tofts PS, Miller DH, Thompson AJ. Variations in T1 and T2 relaxation times of normal appearing white matter and lesions in multiple sclerosis. J Neurol Sci 2000;178(2):81–87. [PubMed: 11018698]
5. Baudrexel S, Nurnberger L, Rub U, Seifried C, Klein JC, Deller T, Steinmetz H, Deichmann R, Hilker R. Quantitative mapping of T1 and T2* discloses nigral and brainstem pathology in early Parkinson's disease. Neuroimage 2010;51(2):512–520. [PubMed: 20211271]
6. Barbosa JHO, Santos AC, Tumas V, Liu MJ, Zheng WL, Haacke EM, Salmon CEG. Quantifying brain iron deposition in patients with Parkinson's disease using quantitative susceptibility mapping, R2 and R2. Magnetic Resonance Imaging 2015;33(5):559–565. [PubMed: 25721997]
7. Li X, Harrison DM, Liu H, Jones CK, Oh J, Calabresi PA, van Zijl PC. Magnetic susceptibility contrast variations in multiple sclerosis lesions. J Magn Reson Imaging 2016;43(2):463–473. [PubMed: 26073973]
8. Du G, Lewis MM, Styner M, Shaffer ML, Sen S, Yang QX, Huang X. Combined R2* and diffusion tensor imaging changes in the substantia nigra in Parkinson's disease. Mov Disord 2011;26(9):1627–1632. [PubMed: 21618607]
9. Helms G, Dathe H, Dechent P. Quantitative FLASH MRI at 3T using a rational approximation of the Ernst equation. Magn Reson Med 2008;59(3):667–672. [PubMed: 18306368]
10. Ben-Eliezer N, Sodickson DK, Block KT. Rapid and accurate T2 mapping from multi-spin-echo data using Bloch-simulation-based reconstruction. Magn Reson Med 2015;73(2):809–817. [PubMed: 24648387]
11. Haacke EM, Liu S, Buch S, Zheng W, Wu D, Ye Y. Quantitative susceptibility mapping: current status and future directions. Magn Reson Imaging 2015;33(1):1–25. [PubMed: 25267705]
12. Betts MJ, Acosta-Cabronero J, Cardenas-Blanco A, Nestor PJ, Duzel E. High-resolution characterisation of the aging brain using simultaneous quantitative susceptibility mapping (QSM) and R-2* measurements at 7 T. Neuroimage 2016;138:43–63. [PubMed: 27181761]
13. Ghadery C, Pirpamer L, Hofer E, Langkammer C, Petrovic K, Loitfelder M, Schwingenschuh P, Seiler S, Duering M, Jouvent E, Schmidt H, Fazekas F, Mangin JF, Chabriat H, Dichgans M, Ropele S, Schmidt R. R2*mapping for brain iron: associations with cognition in normal aging. Neurobiol Aging 2015;36(2):925–932. [PubMed: 25443291]
14. Feng X, Deistung A, Reichenbach JR. Quantitative susceptibility mapping (QSM) and R-2* in the human brain at 3 T Evaluation of intra-scanner repeatability. Zeitschrift Fur Medizinische Physik 2018;28(1):36–48. [PubMed: 28601374]
15. Chen Y, Liu S, Wang Y, Kang Y, Haacke EM. STrategically Acquired Gradient Echo (STAGE) imaging, part I: Creating enhanced T1 contrast and standardized susceptibility weighted imaging and quantitative susceptibility mapping. Magn Reson Imaging 2018;46:130–139. [PubMed: 29056394]
16. Haacke EM, Chen Y, Utriainen D, Wu B, Wang Y, Xia S, He N, Zhang C, Wang X, Lagana MM, Luo Y, Fatemi A, Liu S, Gharabaghi S, Wu D, Sethi SK, Huang F, Sun T, Qu F, Yadav BK, Ma X, Bai Y, Wang M, Cheng J, Yan F. STrategically Acquired Gradient Echo (STAGE) imaging, part III: Technical advances and clinical applications of a rapid multi-contrast multi-parametric brain imaging method. Magn Reson Imaging 2019;65:15–26. [PubMed: 31629075]

17. Wang Y, Chen Y, Wu D, Wang Y, Sethi SK, Yang G, Xie H, Xia S, Haacke EM. STrategically Acquired Gradient Echo (STAGE) imaging, part II: Correcting for RF inhomogeneities in estimating T1 and proton density. Magn Reson Imaging 2018;46:140–150. [PubMed: 29061370]
18. Metere R, Kober T, Moller HE, Schafer A. Simultaneous Quantitative MRI Mapping of T1, T2* and Magnetic Susceptibility with Multi-Echo MP2RAGE. PLoS One 2017;12(1):e0169265. [PubMed: 28081157]
19. Sun HF, Cleary JO, Glarin R, Kolbe SC, Ordidge RJ, Moffat BA, Pike GB. Extracting more for less: multi-echo MP2RAGE for simultaneous T-1-weighted imaging, T-1 mapping, R2*mapping, SWI, and QSM from a single acquisition. Magnet Reson Med 2020;83(4):1178–1191.
20. Caan MW, Bazin PL, Marques JP, de Hollander G, Dumoulin SO, van der Zwaag W. MP2RAGEME: T1, T2*, and QSM mapping in one sequence at 7 tesla. Human brain mapping 2019;40(6):1786–1798. [PubMed: 30549128]
21. Deichmann R, Good CD, Josephs O, Ashburner J, Turner R. Optimization of 3-D MP-RAGE sequences for structural brain imaging. Neuroimage 2000;12(1):112–127. [PubMed: 10875908]
22. Marques JP, Kober T, Krueger G, van der Zwaag W, Van de Moortele PF, Gruetter R. MP2RAGE, a self bias-field corrected sequence for improved segmentation and T1-mapping at high field. Neuroimage 2010;49(2):1271–1281. [PubMed: 19819338]
23. Wang CY, Coppo S, Mehta BB, Seiberlich N, Yu X, Griswold MA. Magnetic resonance fingerprinting with quadratic RF phase for measurement of T-2* simultaneously with delta(f),T-1, and T-2. Magnet Reson Med 2019;81(3):1849–1862.
24. Schweser F, Deistung A, Reichenbach JR. Foundations of MRI phase imaging and processing for Quantitative Susceptibility Mapping (QSM). Z Med Phys 2016;26(1):6–34. [PubMed: 26702760]
25. Wu DM, Liu SF, Buch S, Ye YQ, Dai YM, Haacke EM. A Fully Flow-Compensated Multiecho Susceptibility-Weighted Imaging Sequence: The Effects of Acceleration and Background Field on Flow Compensation. Magnet Reson Med 2016;76(2):478–489.
26. Xu B, Liu T, Spincemaille P, Prince M, Wang Y. Flow compensated quantitative susceptibility mapping for venous oxygenation imaging. Magn Reson Med 2014;72(2):438–445. [PubMed: 24006187]
27. Liang Z-P. Spatiotemporal imagingwith partially separable functions. 2007. IEEE. p 988–991.
28. He JF, Liu QG, Christodoulou AG, Ma C, Lam F, Liang ZP. Accelerated High-Dimensional MR Imaging With Sparse Sampling Using Low-Rank Tensors. Ieee T Med Imaging 2016;35(9):2119–2129.
29. Tucker LR. Some mathematical notes on three-mode factor analysis. Psychometrika 1966;31(3):279–311. [PubMed: 5221127]
30. Kolda TG, Bader BW. Tensor Decompositions and Applications. Siam Review 2009;51(3):455–500.
31. Christodoulou AG, Shaw JL, Nguyen C, Yang Q, Xie Y, Wang N, Li D. Magnetic resonance multitasking for motion-resolved quantitative cardiovascular imaging. Nat Biomed Eng 2018;2(4):215–226. [PubMed: 30237910]
32. De Lathauwer L, De Moor B, Vandewalle J. A multilinear singular value decomposition. Siam J Matrix Anal A 2000;21(4):1253–1278.
33. Abdul-Rahman HS, Gdeisat MA, Burton DR, Lalor MJ, Lilley F, Moore CJ. Fast and robust three-dimensional best path phase unwrapping algorithm. Appl Optics 2007;46(26):6623–6635.
34. Smith SM. Fast robust automated brain extraction. Hum Brain Mapp 2002;17(3):143–155. [PubMed: 12391568]
35. Schweser F, Deistung A, Lehr BW, Reichenbach JR. Quantitative imaging of intrinsic magnetic tissue properties using MRI signal phase: an approach to in vivo brain iron metabolism? Neuroimage 2011;54(4):2789–2807. [PubMed: 21040794]
36. Haacke EM, Tang J, Neelavalli J, Cheng YCN. Susceptibility Mapping as a Means to Visualize Veins and Quantify Oxygen Saturation. Journal of Magnetic Resonance Imaging 2010;32(3):663–676. [PubMed: 20815065]
37. Tang J, Liu S, Neelavalli J, Cheng YCN, Buch S, Haacke EM. Improving Susceptibility Mapping Using a Threshold-Based K-Space/Image Domain Iterative Reconstruction Approach. Magnet Reson Med 2013;69(5):1396–1407.

38. Gharabaghi S, Liu SF, Wang Y, Chen YS, Buch S, Jokar M, Wischgoll T, Kashou NH, Zhang CY, Wu B, Cheng JL, Haacke EM. Multi-Echo Quantitative Susceptibility Mapping for Strategically Acquired Gradient Echo (STAGE) Imaging. Frontiers in Neuroscience 2020;14.
39. Deoni SCL, Rutt BK, Peters TM. Rapid combined T-1 and T-2 mapping using gradient recalled acquisition in the steady state. Magnet Reson Med 2003;49(3):515–526.
40. Shi XF, Kim SE, Jeong EK. Single-Shot T-1 Mapping Using Simultaneous Acquisitions of Spin- and Stimulated-Echo-Planar Imaging (2D ss-SESTEPI). Magnet Reson Med 2010;64(3):734–742.
41. Knight MJ, McCann B, Tsivos D, Dillon S, Coulthard E, Kauppinen RA. Quantitative T2 mapping of white matter: applications for ageing and cognitive decline. Physics in Medicine and Biology 2016;61(15):5587–5605. [PubMed: 27384985]
42. Hattingen E, Jurcoane A, Bahr O, Rieger J, Magerkurth J, Anti S, Steinbach JP, Pilatus U. Bevacizumab impairs oxidative energy metabolism and shows antitumoral effects in recurrent glioblastomas: a P-31/H-1 MRSI and quantitative magnetic resonance imaging study. Neuro-Oncology 2011;13(12):1349–1363. [PubMed: 21890539]
43. Hilbert T, Sumpf TJ, Weiland E, Frahm J, Thiran JP, Meuli R, Kober T, Krueger G. Accelerated T-2 mapping combining parallel MRI and model-based reconstruction: GRAPPATINI. Journal of Magnetic Resonance Imaging 2018;48(2):359–368. [PubMed: 29446508]
44. Haacke EM, Xu Y, Cheng YC, Reichenbach JR. Susceptibility weighted imaging (SWI). Magn Reson Med 2004;52(3):612–618. [PubMed: 15334582]
45. Liu S, Mok K, Neelavalli J, Cheng YC, Tang J, Ye Y, Haacke EM. Improved MR venography using quantitative susceptibility-weighted imaging. J Magn Reson Imaging 2014;40(3):698–708. [PubMed: 24923249]
46. Ma S, Wang N, Fan ZY, Kaisey M, Sicotte NL, Christodoulou AG, Li DB. Three-dimensional whole-brain simultaneous T1, T2, and T1 rho quantification using MR Multitasking: Method and initial clinical experience in tissue characterization of multiple sclerosis. Magnet Reson Med 2021;85(4):1938–1952.
47. de Rochefort L, Brown R, Prince MR, Wang Y. Quantitative MR susceptibility mapping using piece-wise constant regularized inversion of the magnetic field. Magn Reson Med 2008;60(4):1003–1009. [PubMed: 18816834]
48. Chu SC, Xu Y, Balschi JA, Springer CS Jr. Bulk magnetic susceptibility shifts in NMR studies of compartmentalized samples: use of paramagnetic reagents. Magn Reson Med 1990;13(2):239–262. [PubMed: 2156125]
49. Deh K, Kawaji K, Bulk M, Van Der Weerd L, Lind E, Spincemaille P, McCabe Gillen K, Van Auderkerke J, Wang Y, Nguyen TD. Multicenter reproducibility of quantitative susceptibility mapping in a gadolinium phantom using MEDI+0 automatic zero referencing. Magn Reson Med 2019;81(2):1229–1236. [PubMed: 30284727]
50. Wansapura JP, Holland SK, Dunn RS, Ball WS. NMR relaxation times in the human brain at 3.0 tesla. Jmri-J Magn Reson Im 1999;9(4):531–538.
51. Stanisz GJ, Odrobina EE, Pun J, Escaravage M, Graham SJ, Bronskill MJ, Henkelman RM. T1, T2 relaxation and magnetization transfer in tissue at 3T. Magnetic Resonance in Medicine: An Official Journal of the International Society for Magnetic Resonance in Medicine 2005;54(3):507–512.
52. Weiskopf N, Suckling J, Williams G, Correia MM, Inkster B, Tait R, Ooi C, Bullmore ET, Lutti A. Quantitative multi-parameter mapping of R1, PD*, MT, and R2* at 3T: a multi-center validation. Frontiers in neuroscience 2013;7:95. [PubMed: 23772204]
53. Lu HZ, Nagae-Poetscher LM, Golay X, Lin D, Pomper M, van Zijl PCM. Routine clinical brain MRI sequences for use at 3.0 Tesla. Journal of Magnetic Resonance Imaging 2005;22(1):13–22. [PubMed: 15971174]
54. Wang XQ, Voit D, Roeloffs V, Uecker M, Frahm J. Fast Interleaved Multislice T1 Mapping: Model-Based Reconstruction of Single-Shot Inversion-Recovery Radial FLASH. Comput Math Method M 2018;2018.
55. Gelman N, Ewing JR, Gorell JM, Spickler EM, Solomon EG. Interregional variation of longitudinal relaxation rates in human brain at 3.0 T: Relation to estimated iron and water contents. Magnet Reson Med 2001;45(1):71–79.

56. Gelman N, Gorell JM, Barker PB, Savage RM, Spickler EM, Windham JP, Knight RA. MR imaging of human brain at 3.0 T: Preliminary report on transverse relaxation rates and relation to estimated iron content. Radiology 1999;210(3):759–767. [PubMed: 10207479]
57. Cicchetti DV. Guidelines, criteria, and rules of thumb for evaluating normed and standardized assessment instruments in psychology. Psychological assessment 1994;6(4):284.
58. Lim IAL, Faria AV, Li X, Hsu JTC, Airan RD, Mori S, van Ziji PCM. Human brain atlas for automated region of interest selection in quantitative susceptibility mapping: Application to determine iron content in deep gray matter structures. Neuroimage 2013;82:449–469. [PubMed: 23769915]
59. Chai C, Yan S, Chu ZQ, Wang T, Wang LJ, Zhang MJ, Zuo C, Haacke EM, Xia S, Shen W. Quantitative measurement of brain iron deposition in patients with haemodialysis using susceptibility mapping. Metab Brain Dis 2015;30(2):563–571. [PubMed: 25182196]
60. He NY, Ling HW, Ding B, Huang J, Zhang Y, Zhang ZP, Liu CL, Chen KM, Yan FH. Region-specific disturbed iron distribution in early idiopathic Parkinson's disease measured by quantitative susceptibility mapping. Human Brain Mapping 2015;36(11):4407–4420. [PubMed: 26249218]
61. Schweser F, Deistung A, Lehr BW, Reichenbach JR. Quantitative imaging of intrinsic magnetic tissue properties using MRI signal phase: An approach to in vivo brain iron metabolism? Neuroimage 2011;54(4):2789–2807. [PubMed: 21040794]
62. Kim D, Wisnowski JL, Nguyen CT, Haldar JP. Probing in Vivo Microstructure with T 1-T 2 Relaxation Correlation Spectroscopic Imaging. Proc IEEE Int Symp Biomed Imaging 2018;2018:675–678. [PubMed: 30854157]
63. Istratov AA, Vyvenko OF. Exponential analysis in physical phenomena. Rev Sci Instrum 1999;70(2):1233–1257.
64. Epstein CL, Schotland J. The bad truth about Laplace's transform. Siam Review 2008;50(3):504–520.
65. Kim D, Wisnowski JL, Nguyen CT, Haldar JP. Multidimensional correlation spectroscopic imaging of exponential decays: From theoretical principles to in vivo human applications. NMR Biomed 2020;33(12):e4244. [PubMed: 31909534]
66. Sati P, Oh J, Constable RT, Evangelou N, Guttmann CR, Henry RG, Klawiter EC, Mainero C, Massacesi L, McFarland H, Nelson F, Ontaneda D, Rauscher A, Rooney WD, Samaraweera AP, Shinohara RT, Sobel RA, Solomon AJ, Treaba CA, Wuerfel J, Zivadinov R, Sicotte NL, Pelletier D, Reich DS, Cooperative N. The central vein sign and its clinical evaluation for the diagnosis of multiple sclerosis: a consensus statement from the North American Imaging in Multiple Sclerosis Cooperative. Nat Rev Neurol 2016;12(12):714–722. [PubMed: 27834394]
67. Ellingson BM, Bendszus M, Boxerman J, Barboriak D, Erickson BJ, Smits M, Nelson SJ, Gerstner E, Alexander B, Goldmacher G, Wick W, Vogelbaum M, Weller M, Galanis E, Kalpathy-Cramer J, Shankar L, Jacobs P, Pope WB, Yang D, Chung C, Knopp MV, Cha S, van den Bent MJ, Chang S, Yung WK, Cloughesy TF, Wen PY, Gilbert MR, Jumpstarting Brain Tumor Drug Development Coalition Imaging Standardization Steering C. Consensus recommendations for a standardized Brain Tumor Imaging Protocol in clinical trials. Neuro Oncol 2015;17(9):1188–1198. [PubMed: 26250565]
68. Traboulsee A, Simon JH, Stone L, Fisher E, Jones DE, Malhotra A, Newsome SD, Oh J, Reich DS, Richert N, Rammohan K, Khan O, Radue EW, Ford C, Halper J, Li D. Revised Recommendations of the Consortium of MS Centers Task Force for a Standardized MRI Protocol and Clinical Guidelines for the Diagnosis and Follow-Up of Multiple Sclerosis. AJNR Am J Neuroradiol 2016;37(3):394–401. [PubMed: 26564433]
69. Zhu DC, Penn RD. Full-brain T1 mapping through inversion recovery fast spin echo imaging with time-efficient slice ordering. Magnetic Resonance in Medicine: An Official Journal of the International Society for Magnetic Resonance in Medicine 2005;54(3):725–731.
70. Jiang Y, Ma D, Keenan KE, Stupic KF, Gulani V, Griswold MA. Repeatability of magnetic resonance fingerprinting T1 and T2 estimates assessed using the ISMRM/NIST MRI system phantom. Magn Reson Med 2017;78(4):1452–1457. [PubMed: 27790751]
71. McPhee KC, Wilman AH. Limitations of skipping echoes for exponential T2 fitting. J Magn Reson Imaging 2018;48(5):1432–1440. [PubMed: 29687931]

72. Wang K, Doneva M, Amthor T, Keil VC, Karasan E, Tan F, Tamir JI, Yu SX, Lustig M. High Fidelity Direct-Contrast Synthesis from Magnetic Resonance Fingerprinting in Diagnostic Imaging. 2020; Paris.

73. Tanenbaum LN, Tsiouris AJ, Johnson AN, Naidich TP, DeLano MC, Melhem ER, Quarterman P, Parameswaran SX, Shankaranarayanan A, Goyen M, Field AS. Synthetic MRI for Clinical Neuroimaging: Results of the Magnetic Resonance Image Compilation (MAGiC) Prospective, Multicenter, Multireader Trial. Am J Neuroradiol 2017;38(6):1103–1110. [PubMed: 28450439]

74. Qiu S, Chen Y, Ma S, Fan Z, Moser FG, Maya MM, Christodoulou AG, Xie Y, Li D. Multiparametric mapping in the brain from conventional contrast-weighted images using deep learning. Magn Reson Med 2021.

75. Chen Y, Fang Z, Hung S-C, Chang W-T, Shen D, Lin W. High-resolution 3D MR Fingerprinting using parallel imaging and deep learning. NeuroImage 2020;206:116329. [PubMed: 31689536]

76. Kim TH, Setsompop K, Haldar JP. LORAKS Makes Better SENSE: Phase-Constrained Partial Fourier SENSE Reconstruction Without Phase Calibration. Magnet Reson Med 2017;77(3):1021–1035.

77. Kustner T, Bustin A, Jaubert O, Hajhosseiny R, Masci PG, Neji R, Botnar R, Prieto C. Isotropic 3D Cartesian single breath-hold CINE MRI with multi-bin patch-based low-rank reconstruction. Magnet Reson Med 2020;84(4):2018–2033.

78. Pham CH, Tor-Diez C, Meunier H, Bednarek N, Fablet R, Passat N, Rousseau F. Multiscale brain MRI super-resolution using deep 3D convolutional networks. Comput Med Imag Grap 2019;77.

79. Chen Y, Shi F, Christodoulou AG, Xie Y, Zhou Z, Li D. Efficient and accurate MRI super-resolution using a generative adversarial network and 3D multi-level densely connected network. 2018. Springer. p 91–99.

80. Afacan O, Erem B, Roby DP, Roth N, Roth A, Prabhu SP, Warfield SK. Evaluation of motion and its effect on brain magnetic resonance image quality in children. Pediatr Radiol 2016;46(12):1728–1735. [PubMed: 27488508]

81. Godenschweger F, Kagebein U, Stucht D, Yarach U, Sciarra A, Yakupov R, Lusebrink F, Schulze P, Speck O. Motion correction in MRI of the brain. Phys Med Biol 2016;61(5):R32–56. [PubMed: 26864183]

82. Ma S, Wang N, Xie Y, Fan Z, Li D, Christodoulou AG. Motion-robust quantitative multiparametric brain MRI with motion-resolved MR multitasking. Magn Reson Med 2021.

83. Ma S, Nguyen CT, Han F, Wang N, Deng Z, Binesh N, Moser FG, Christodoulou AG, Li D. Three-dimensional simultaneous brain T1, T2, and ADC mapping with MR Multitasking. Magn Reson Med 2020;84(1):72–88. [PubMed: 31765496]

84. Wang N, Christodoulou AG, Xie YB, Wang ZJ, Deng ZX, Zhou B, Lee S, Fan ZY, Chang H, Yu W, Li DB. Quantitative 3D dynamic contrast-enhanced (DCE) MR imaging of carotid vessel wall by fast T1 mapping using Multitasking. Magnet Reson Med 2019;81(4):2302–2314.

85. Han P, Zhang R, Wagner S, Xie YB, Cingolani E, Marban E, Christodoulou AG, Li DB. Electrocardiogram-less, free-breathing myocardial extracellular volume fraction mapping in small animals at high heart rates using motion-resolved cardiovascular magnetic reesonance multitasking: a feasibility study in a heart failure with preserved ejection fraction rat model. J Cardiovasc Magn R 2021;23(1).

86. Hu ZH, Christodoulou AG, Wang N, Shaw JL, Song SS, Maya MM, Ishimori ML, Forbess LJ, Xiao JY, Bi XM, Han F, Li DB, Fan ZY. Magnetic resonance multitasking for multidimensional assessment of cardiovascular system: Development and feasibility study on the thoracic aorta. Magnet Reson Med 2020;84(5):2376–2388.

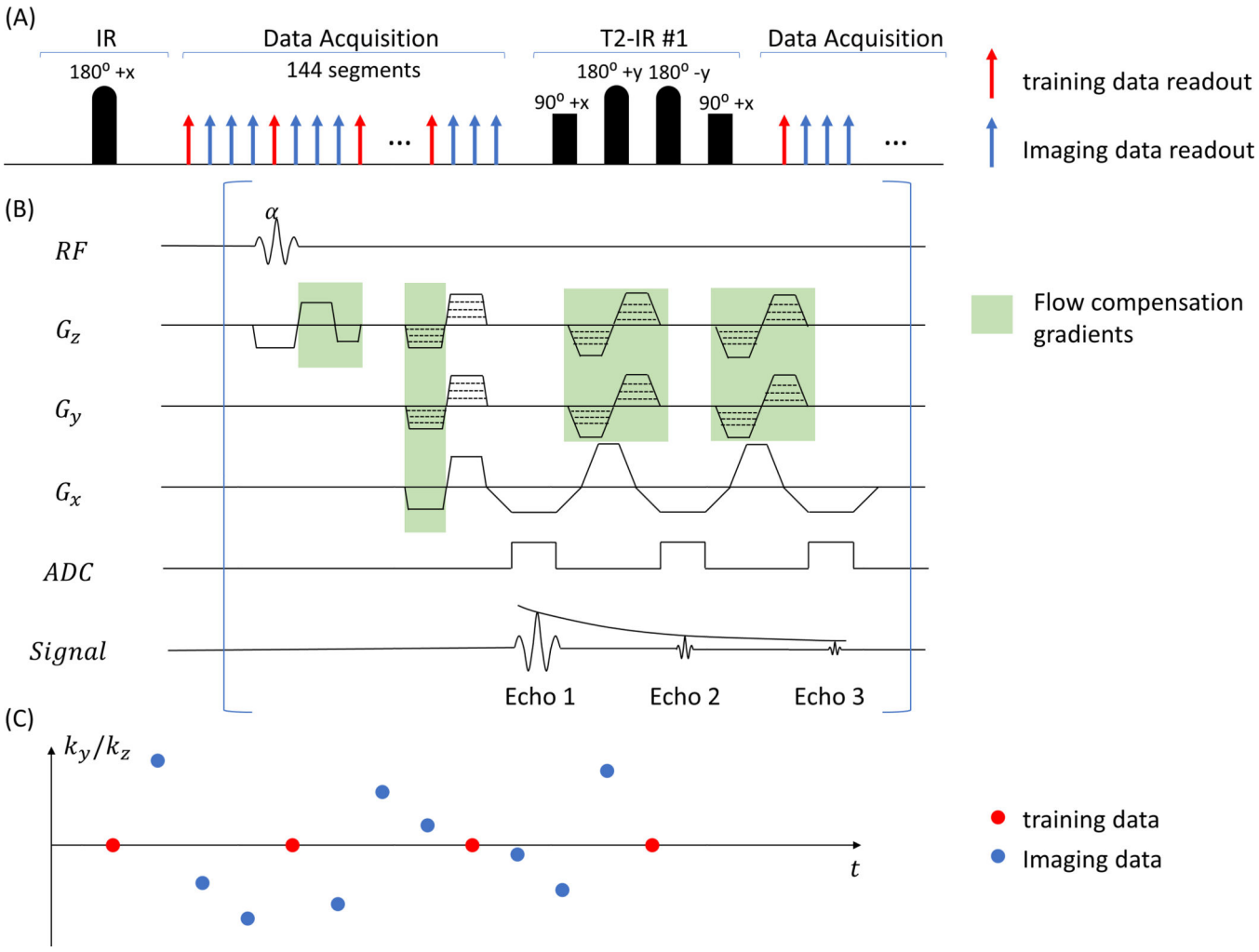

Figure 1.

(A) Sequence diagram for the proposed multitasking T1/T2/T2* mapping framework. Hybrid T2prep/IR (T2-IR) preparation modules were followed by 144 multi-echo GRE readouts, which enable collection of k-space lines with different T1/T2/T2* contrasts. The training data was acquired every 4 readouts.

(B) Illustration of readout module. After each α pulse, a total of 3 echoes, each of them fully flow compensated along all directions, were collected in a monopolar way. In the readout direction, each echo is refocused, and flow compensation is naturally achieved at the center of each echo after inserting an appropriate moment nulling gradient before the first echo. In the phase/partition encoding direction, however, bipolar gradient pairs were added for all later echoes.

(C) Simplified illustration of k-space sampling pattern. Cartesian acquisition with random Gaussian distribution was adopted along k_y and k_z axis. k-Space center was acquired every 4 readouts and would serve for tracking temporal dynamics.

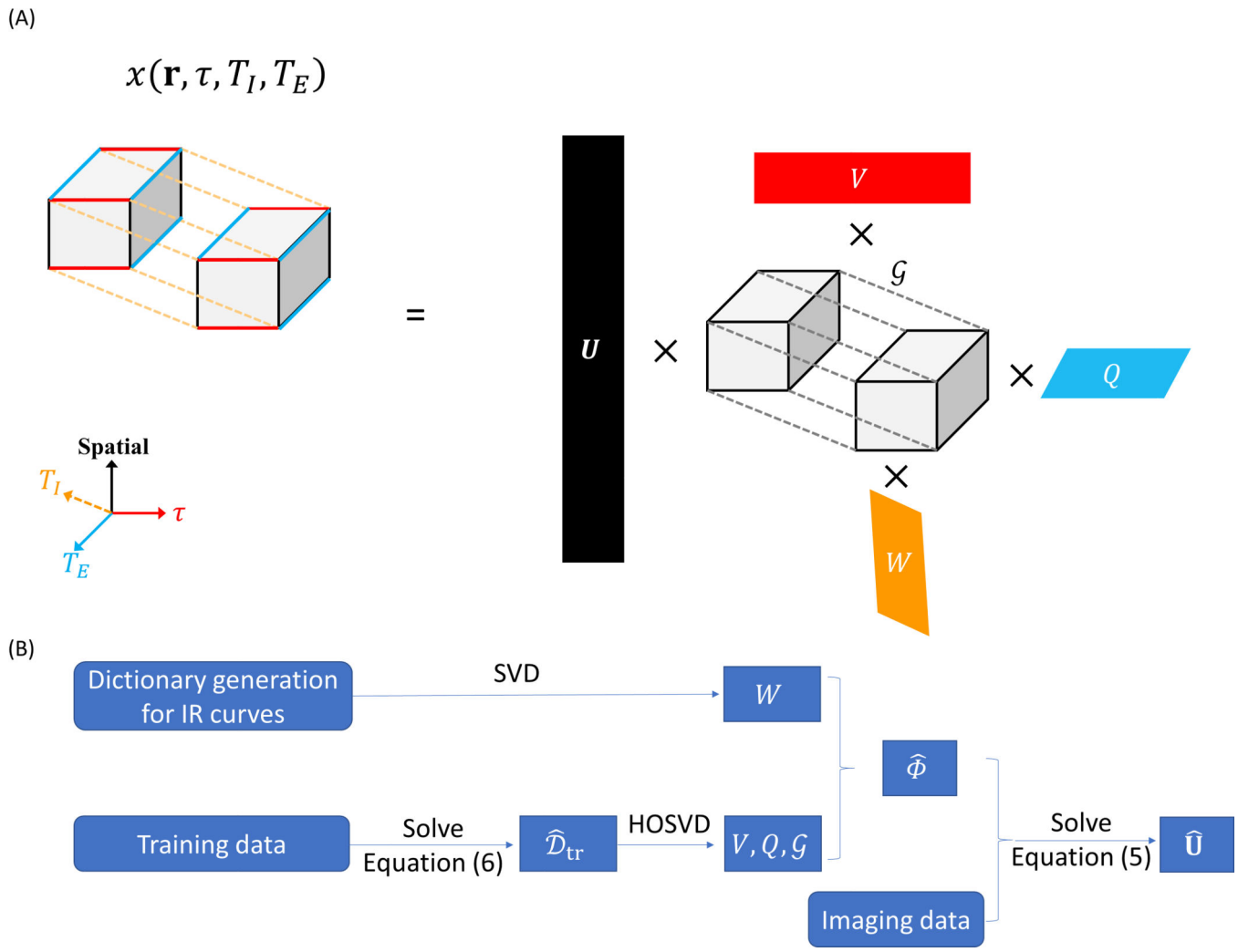

Figure 2.

(A) Illustration of multiple temporal dimensions of the low-rank tensor for simultaneous T1, T2, T2*, and susceptibility mapping. The image tensor contains spatial, T2IR preparation duration τ, inversion time T_I, echo time T_E dimensions, with size [$N_x \cdot N_y \cdot N_z$, 4, 144, 3]. The low-rank tensor structure can be explicitly expressed through tensor factorization between 4 sets of basis functions (**U** with size [$N_x \cdot N_y \cdot N_z$, L], V with size [4, M], $\boldsymbol{W}$ with size [144, N], $\boldsymbol{Q}$ with size [3, P]) assigned to each dimension and a core tensor ($\mathcal{G}$ with size [L, M, N, P]) governing the interaction between different basis functions.

(B) Reconstruction workflow. The reconstructed tensor is given by $\widehat{\mathcal{X}} = \widehat{\boldsymbol{\Phi}} \times_1 \widehat{\mathbf{U}}$.

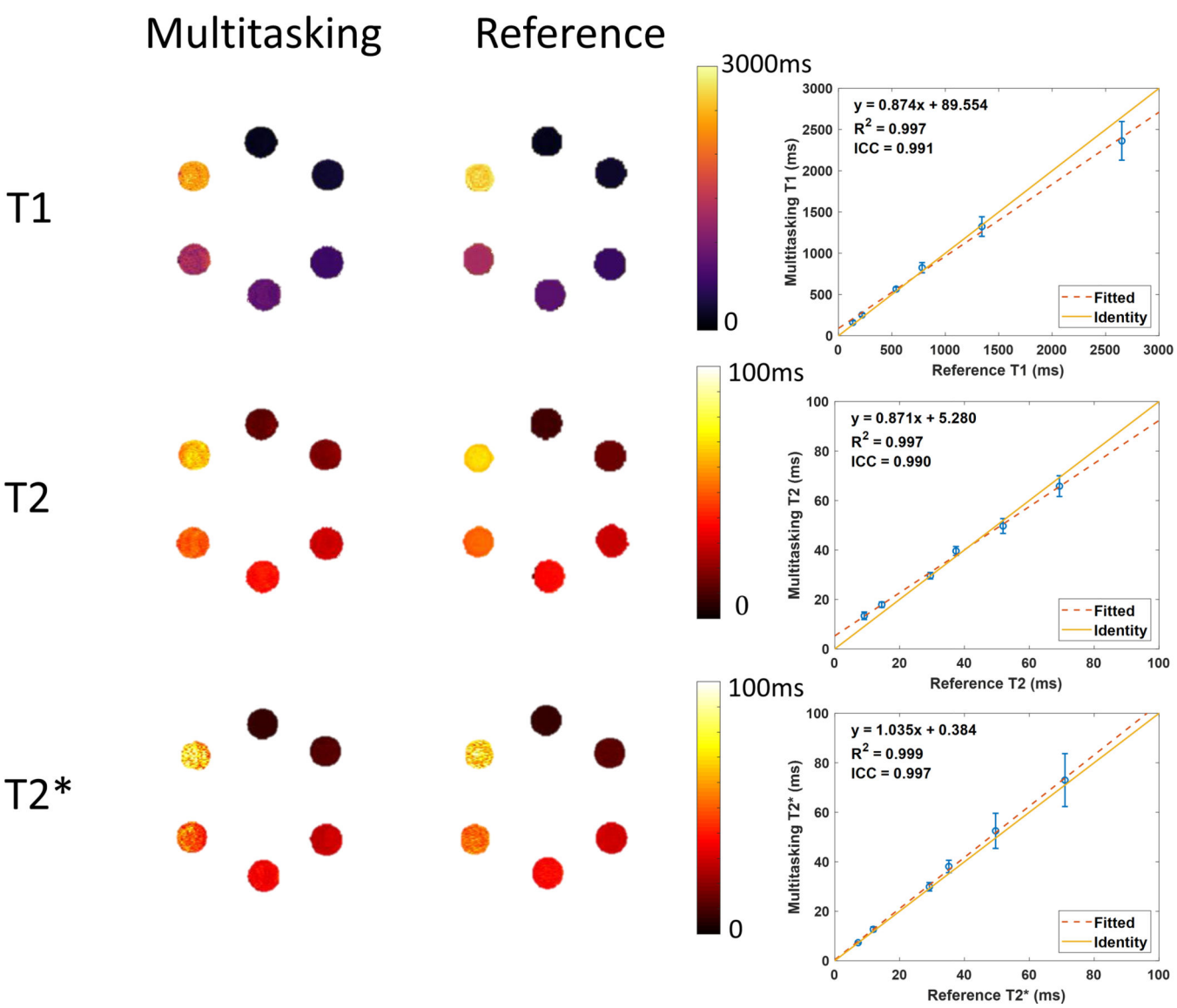

Figure 3.

Comparison between Multitasking and references on a standard phantom. Multitasking shows comparable image quality and correlates well with the references, as denoted by R^2 and ICC. The solid line represents identity (y = x), and the dotted line represents linear regression fitting.

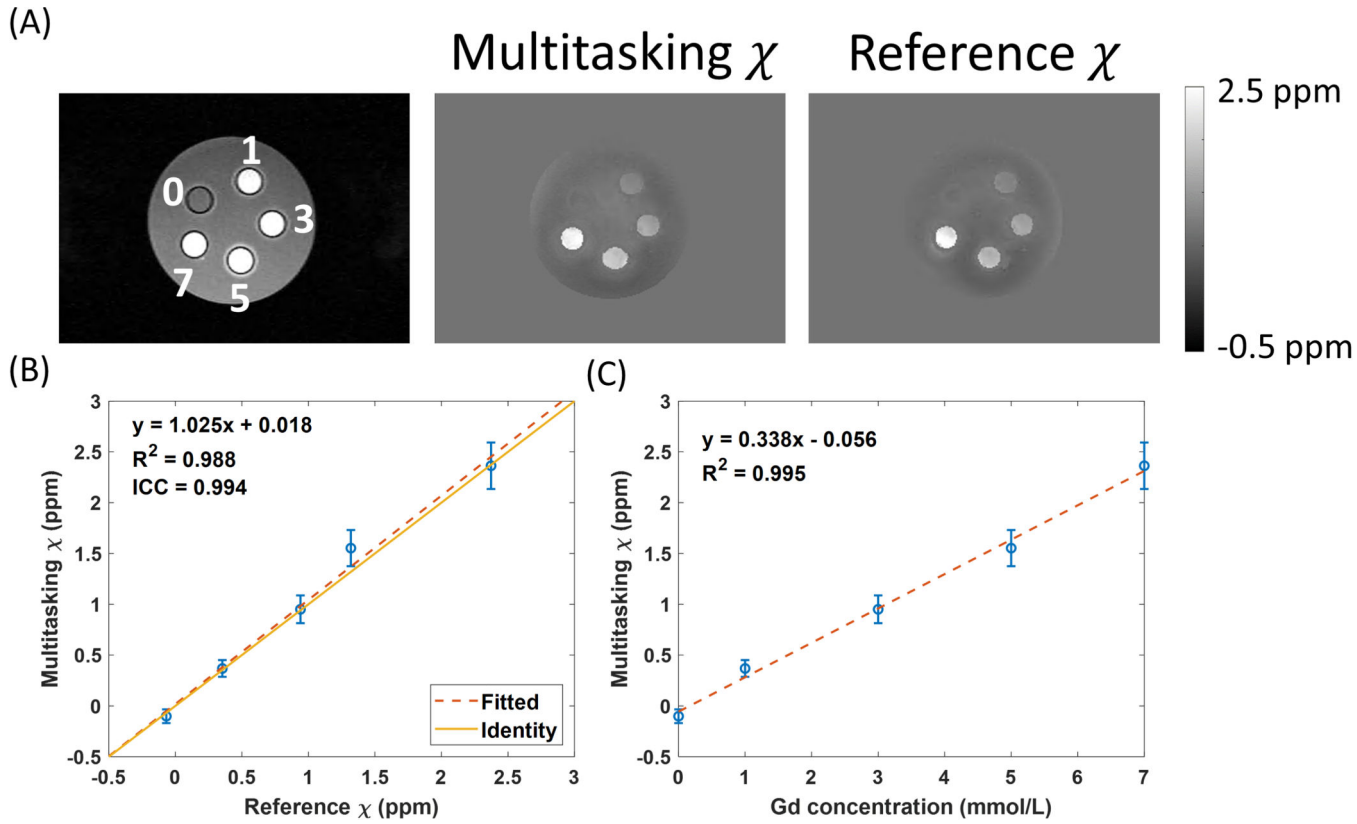

Figure 4.

(A) Comparison of susceptibility map from Multitasking and references on a Gd phantom, with Gd concentration (in mmol/L) labelled for each tube in the magnitude image.

(B) Multitasking susceptibility correlates well with the reference susceptibility, as denoted by R^2 and ICC. The solid line represents identity (y = x), and the dotted line represents linear regression fitting.

(C) Multitasking susceptibility correlates well with the Gd concentration and yields a slope of 0.338 ppm per mmol/L. The dotted line represents linear regression fitting.

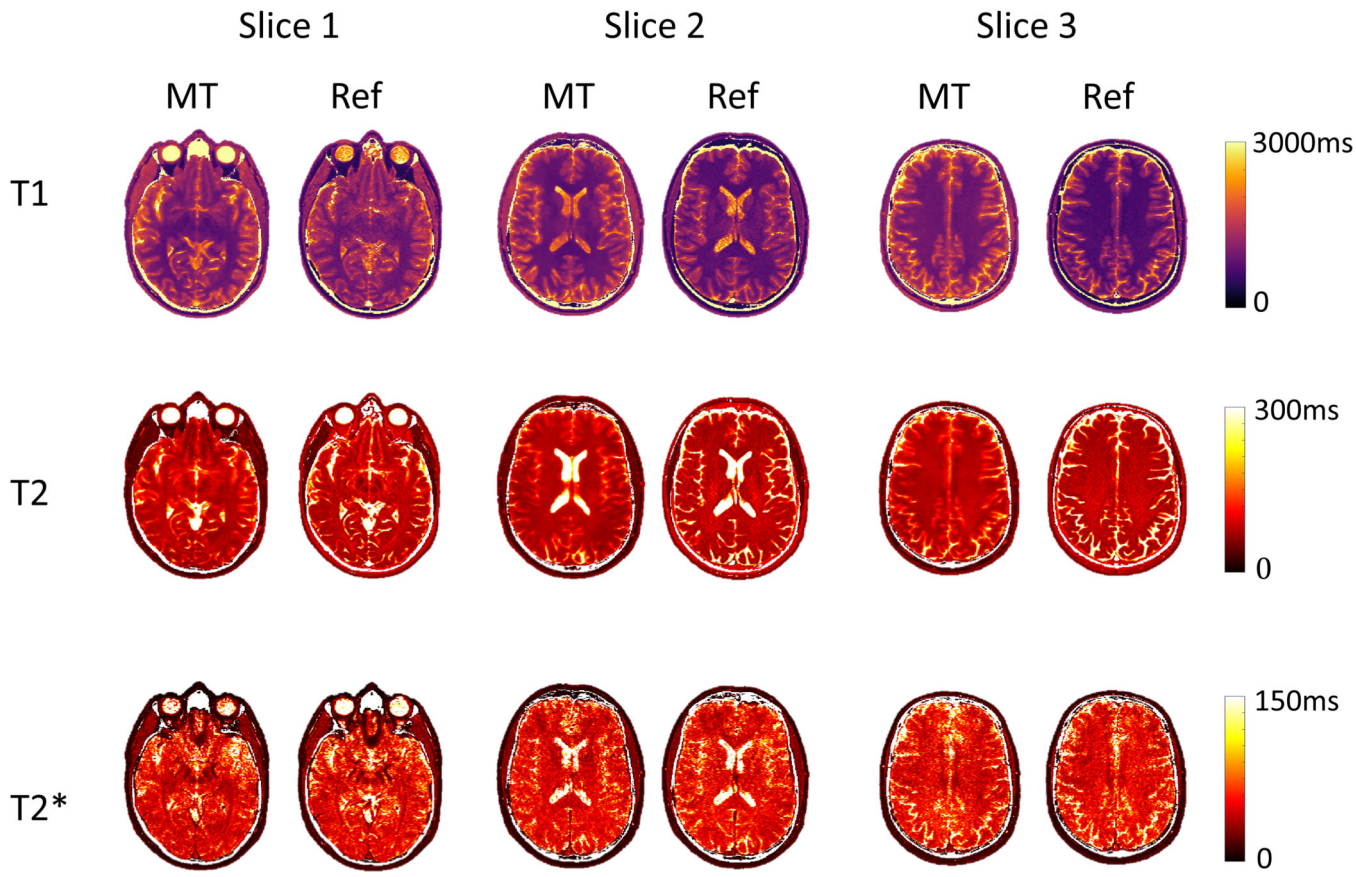

Figure 5.

Representative in-vivo T1/T2/T2* mapping at three slice locations using MR Multitasking (MT) and the corresponding reference (Ref) protocols for a healthy volunteer. Multitasking provides T1/T2/T2* maps with good qualitative agreement with the references.

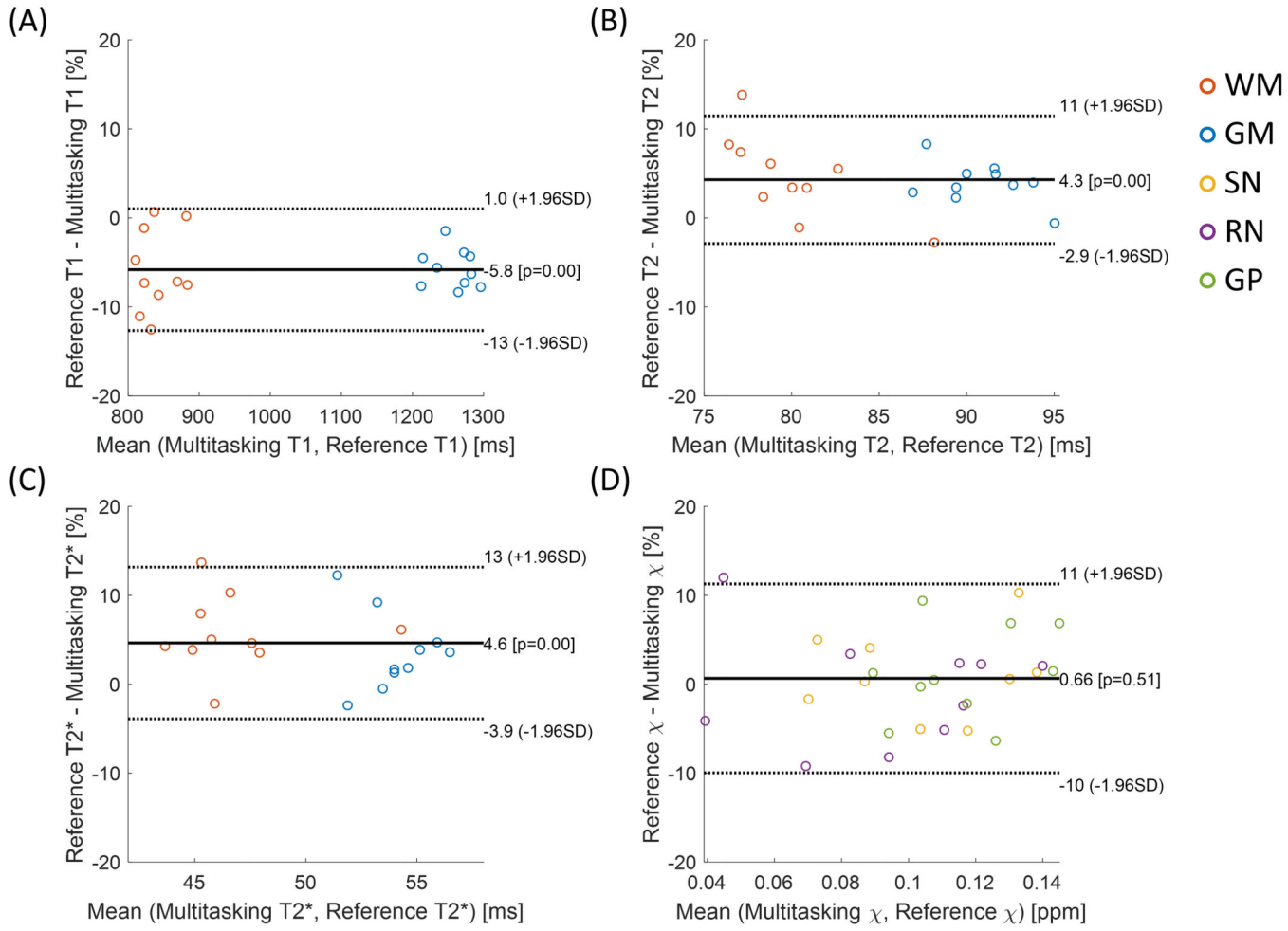

Figure 6.

Bland - Altman plots comparing Multitasking (A) T1, (B) T2, (C) T2*, and (D) susceptibility measurements with those of the references (N=10). The dotted lines represent 95% confidence level. The solid lines represent mean percentage differences.

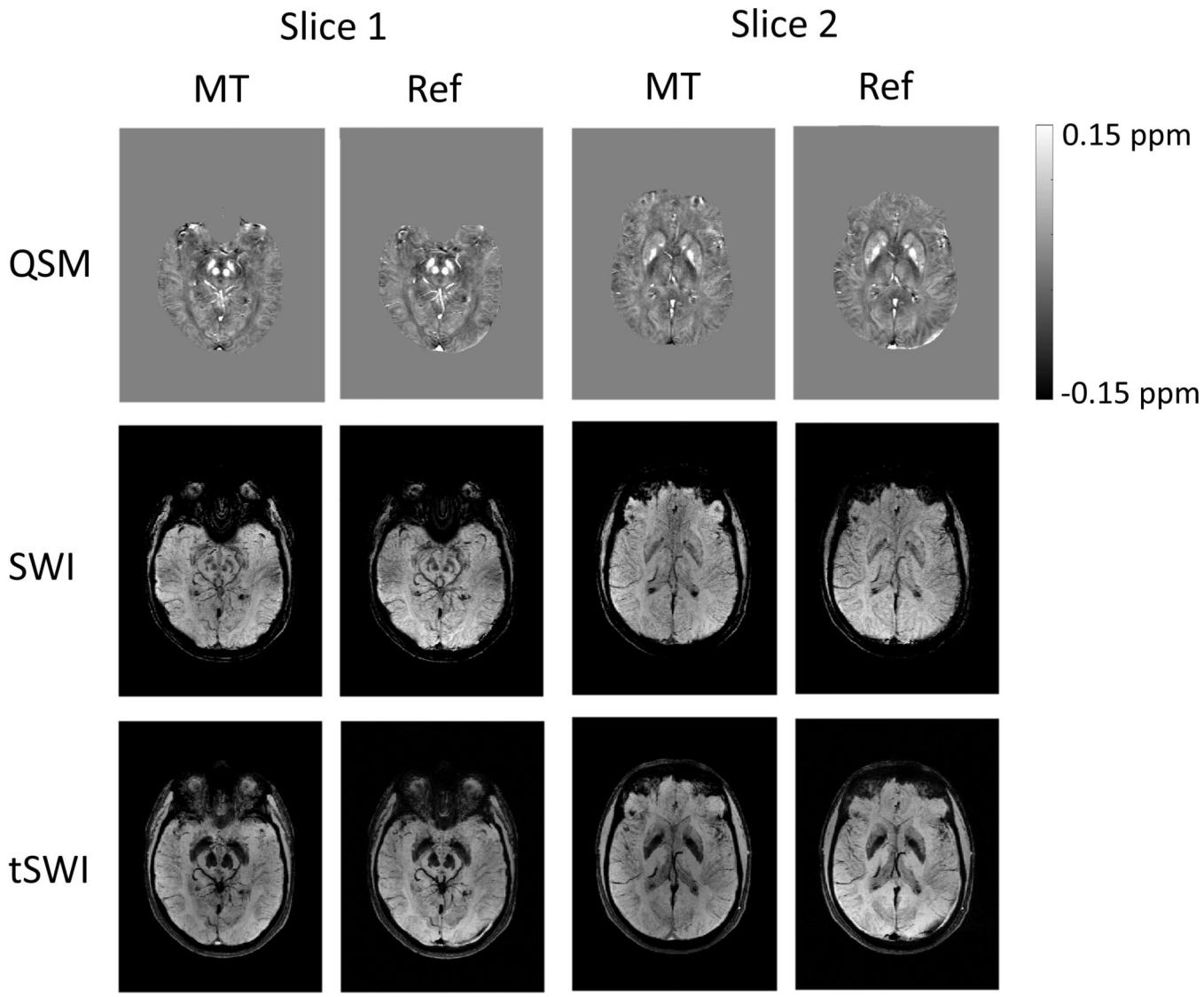

Figure 7.

Representative in-vivo QSM at two slice locations using MR Multitasking (MT) and references (Ref) on the same healthy volunteer. Both QSM and SWI/ tSWI (MinIP) images agreed with the reference in terms of deep gray matter and vessel visualization.

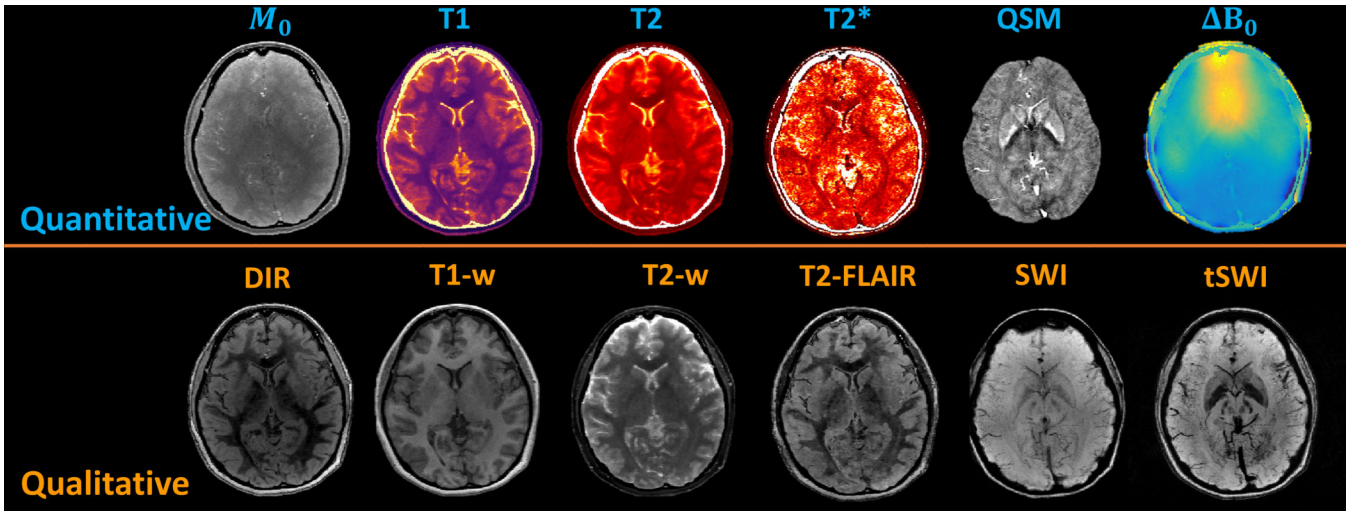

Figure 8.

Results from a healthy volunteer including qualitative images and quantitative maps. The first row included quantitative maps and the second row showed all the weighted images. SWI and tSWI were MinIP results with an effective slab thickness of 16mm.

Table 1.

MR Multitasking T1/T2/T2*/susceptibility mapping protocol

FOV (mm^2)	276 × 207	**Slab thickness (mm)**	144
In-plane resolution (mm^3)	0.7 × 1.4	**Slice thickness (mm)**	2
Scanning matrix	384 × 144	**Number of slices**	72
Recovery period (ms)	2780	**Number of segments**	144
T_R (ms)	19.3	**Echo time (ms)**	5, 10, 16.25
T2 prep duration (ms)	0, 30, 55, 80	**Pixel BW (Hz/pixel)**	482
Flip angle (°)	8	**Number of recovery periods**	192
Scan time (min:sec)	9:08		

Table 2.

T1/T2/T2*/susceptibility measurements of N=10 healthy volunteers using Multitasking and the references along with ICC and CV between different methods.

		Multitasking	Reference	ICC	CV
T1 (ms)	GM	1293.7 ± 35.1	1221.8 ± 29.5	0.950	4.77%
	WM	866.7 ± 30.8	817.0 ± 35.3		
T2 (ms)	GM	89.0 ± 3.2	92.6 ± 2.4	0.781	3.94%
	WM	78.2 ± 5.0	81.8 ± 2.5		
T2* (ms)	GM	53.1 ± 2.1	55.0 ± 1.8	0.794	4.45%
	WM	45.4 ± 3.0	48.1 ± 3.2		
QSM (ppm)	SN	0.108 ± 0.027	0.110 ± 0.029	0.981	3.79%
	RN	0.094 ± 0.034	0.093 ± 0.034		
	GP	0.115 ± 0.019	0.117 ± 0.021		